Frontiers of Information Technology & Electronic Engineering
www.zju.edu.cn/jzus; engineering.cae.cn; www.springerlink.com
ISSN 2095-9184 (print); ISSN 2095-9230 (online)
E-mail: jzus@zju.edu.cn

A space-saving steering method for underwater gliders in lake monitoring*

Yu-shi ZHU, Can-jun YANG†‡, Shi-jun WU, Qing LI, Xiao-le XU

(*The State Key Laboratory of Fluid Power & Mechatronic Systems, Zhejiang University, Hangzhou 310027, China*)

†E-mail: ycj@zju.edu.cn

Received Nov. 16, 2015; Revision accepted Feb. 17, 2016; Crosschecked Mar. 14, 2017

Abstract: An increasing number of underwater gliders have been applied to lake monitoring. Lakes have a limited vertical space. Therefore, good space-saving capacity is required for underwater gliders to enlarge the spacing between monitoring waypoints. This paper presents a space-saving steering method under a small pitch angle (SPA) for appearance-fixed underwater gliders. Steering under an SPA increases the steering angle in per unit vertical space. An amended hydrodynamic model for both small and large attack angles is presented to help analyze the steering process. Analysis is conducted to find the optimal parameters of net buoyancy and roll angle for steering under an SPA. A lake trial with a prototype tiny underwater glider (TUG) is conducted to inspect the applicability of the presented model. The trial results show that steering under an SPA saves vertical space, unlike that under a large pitch angle. Simulation results of steering are consistent with the trial results. In addition, multiple-waypoint trial shows that monitoring with steering under an SPA covers a larger horizontal displacement than that without steering.

Key words: Underwater glider; Lake monitoring; Space-saving; Steering method; Small pitch angle (SPA); Hydrodynamics
http://dx.doi.org/10.1631/FITEE.1500399 **CLC number:** TP242

1 Introduction

Long-term lake monitoring, such as water column monitoring (He *et al.*, 2012), lake nutrient stoichiometry (Li *et al.*, 2014), lake geology (Ivanov *et al.*, 2013), and pollution assessment (Wang *et al.*, 2014), has been receiving increasing interest. The existing approach involving using tethered sensors or remotely operated vehicles (ROVs) from a ship (Lim *et al.*, 2011) is costly. Untethered autonomous underwater vehicles (AUVs) or underwater robotic fishes (Denkenberger *et al*., 2007) can be used for lake monitoring, but for only several hours. Moored probe networks (Bardyshev, 2004) are applicable. However, they are spatially fixed and costly deployed. Underwater gliders are highly efficient. These gliders are characterized by long endurance. Thus, an increasing number of these underwater gliders have been applied to long-term lake monitoring. Suberg *et al*. (2014) assessed the application of an underwater glider for plankton monitoring in shallow water. Austin (2013a) presented the potential for underwater gliders in lake monitoring. Underwater gliders were used for observations in Lake Superior (Austin, 2013b). Weng *et al*. (2015) used an underwater glider to measure microstructure turbulence in a lake. The demand for underwater gliders may exist for long-term lake applications.

To monitor water column data in lakes, an underwater glider cruises between planned waypoints to collect hydrology profile data. Two adjacent waypoints are connected by a single flight and a vertical monitoring process (Fig. 1). A single flight is known to include at least a steering process and a transit flight process (Wang *et al*., 2009). To achieve a large

‡ Corresponding author

* Project supported by the Science Fund for Creative Research Groups of the National Natural Science Foundation of China (No. 51521064) and the National High-Tech R&D Program (863) of China (No. 2014AA09A513)

ORCID: Can-jun YANG, http://orcid.org/0000-0002-3712-0538

horizontal displacement for a single flight, more vertical space should be available. However, lakes always have a limited vertical space. Even worse, a space-consuming steer process would further take up the vertical space for transit flight. To leave more available vertical space for transit flight, efforts have been made to reduce the space that the steering process occupies. A hybrid glider that combines the features of underwater gliders and AUVs achieved enhanced steering performance (Caffaz *et al.*, 2010; Peng *et al.*, 2014). The underwater glider Slocum steered itself with a rudder (Jones *et al.*, 2014). A hybrid-driven underwater glider developed by Universiti Sains Malaysia (USM) was equipped with independently controllable wings and rudder to achieve good maneuverability (Isa and Arshad, 2011). A hybrid gliding robotic fish reduced the steering radius (Zhang *et al.*, 2014). Though gliders with rudders or thrusters have enhanced maneuverability, they may encounter some problems with long-term lake monitoring. First, the risk of rotating sealing failure exists when using rotatable wings or rudders. Several Slocum gliders have detected leaks at the rudders (Leonard *et al.*, 2010). Second, risks may arise when the gliders are monitoring areas with suspended solids, such as industry wastewater. The rotatable rudders or thrusters stir the wastewater, potentially leading to a thruster fault (Ahmadzadeh *et al.*, 2014). In this situation, appearance-fixed underwater gliders, which lack accessories (such as rudders and thrusters), are more reliable. However, few studies have been conducted to reduce the space of the steering process occupied by appearance-fixed underwater gliders. Considering such a research gap, we present a space-saving steering method for appearance-fixed underwater gliders.

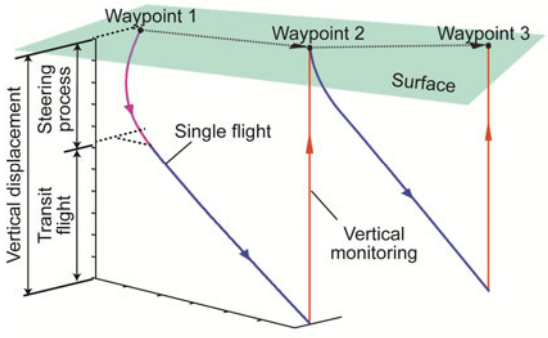

Fig. 1 Schedule diagram of lake monitoring pattern

The main objective of this paper is to present a space-saving steering method under a small pitch angle (SPA) for underwater gliders. Steering with an SPA helps appearance-fixed underwater gliders steer when occupying small vertical displacements. Thus, this approach can save space. When an underwater glider steers under an SPA, the direction of gravity is perpendicular to the axis of the fuselage of the glider. This condition would easily lead to a large attack angle for steering, thereby limiting the increase of axial linear velocity (Yang *et al.*, 2014). When an underwater glider steers with an SPA and a low axial linear velocity, a good trade-off between the steering traction torque and the vertical displacement can be achieved easily.

Models have to be established first to analyze the steering process. Geisbert (2005) presented a model of underwater gliders. The approximate analytical solution for steady spiraling motion was presented by Mahmoudian *et al.* (2010). Zhang *et al.* (2013) modeled the spiraling motion with a recursive algorithm. Zhang *et al.* (2014) quantified the spiraling motion of a gliding robotic fish under a pitch angle from −32.3° to 70.8°. Cao *et al.* (2015) calculated the hydrodynamic coefficients for an attack angle from −10° to 10° and analyzed the steering process under a pitch angle of 48°. Geisbert (2007) and Chen *et al.* (2010) analyzed the hydrodynamics with a maximum attack angle of 20°, which was applied to steering analysis. However, none of these works studied the steering process under an SPA where large attack angles occur. These existing hydrodynamic models somehow become inaccurate under large attack angles. To obtain a more accurate model for underwater gliders under large attack angles, we amend the hydrodynamic model to extend its applicability. In addition, research has been conducted to determine the relationship between the pitch angle, the roll angle, the net buoyancy, and the steering performance through simulations and experiments.

To inspect the applicability of this steering method and the accuracy of the model, a lake trial with a prototype has to be conducted. We designed a small prototype called the tiny underwater glider (TUG), which can adjust the pitch angle for general gliding and vertical ascent. Results of the trial show that this steering method achieves a space-saving steering process, and the model predicts the process well.

2 Principle and prototype

Steering under an SPA aims to achieve a large steering angle when occupying a small vertical displacement as the underwater glider steers. We define the pitch angle as small when the corresponding attack angle is larger than the critical one. Lift force would decrease when the attack angle is beyond the critical angle. When an underwater glider steers under an SPA, the direction of gravity is almost perpendicular to the axis of the fuselage of the glider. This force status would easily lead to a large attack angle for steering, and limit the increase of the axial linear velocity. As a benefit for steering, low linear velocity induces a low drag torque, which would slow down the steering (Wang *et al.*, 2007). Moreover, when the underwater glider steers with an SPA, a large attack angle, a proper roll angle, and a good trade-off can be achieved easily between the steering traction torque and the vertical displacement.

When steering with an SPA, the pitch angle should be kept close to zero, and a roll movement should be performed according to the steering algorithm. To apply the steering process with an SPA to a single flight, the pitch angle should be first kept close to zero for the steering process, and then changed to a suitable value for the transit flight. Fig. 2 shows a brief schedule diagram for the steering process with an SPA and a traditional pitch angle of −20° (Hussain *et al*., 2011).

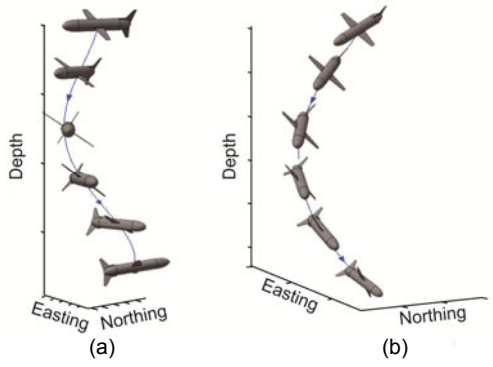

Fig. 2 Steering with (a) and without (b) a small pitch angle

The platform used to inspect the applicability of steering with an SPA and the accuracy of the model is the TUG prototype (Fig. 3a). TUG consists of a ballast module, a sensor module, a gravity center adjustment module (GCAM), and a communication module. The ballast module uses a through-type motor to change the volume of the displaced water. The communication module consists of a free-wave communication module and a Global Positioning System (GPS) module. The sensor part consists of an attitude sensor (TCM-XB, developed by PNI), a gyroscope (3DM-KX10, developed by MARHS), a depth sensor (developed by HUBA), and a temperature probe. GCAM consists of a linear moving platform that supports two rotatable mass blocks. The gravity center of TUG could be adjusted by GCAM in three degrees of freedom, namely, axially linear, radially linear, and circumferentially rotatable. The detailed structure of GCAM is shown in Fig. 3b. The linear moving platform is driven by a through-type

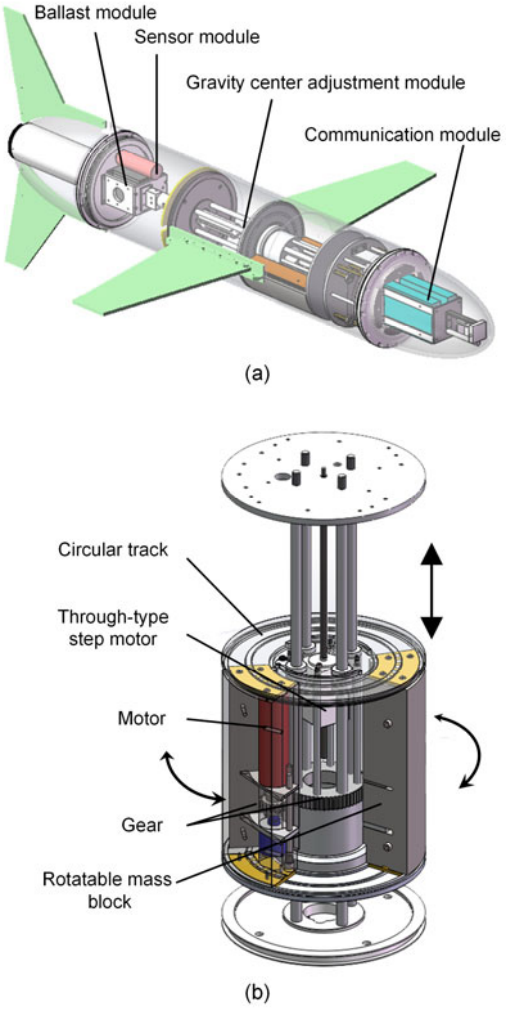

Fig. 3 Tiny underwater glider (a) and gravity center adjustment module (b)

step motor to adjust the gravity center position axially. Each rotatable mass block rotates along the circular track. The included angle of the two mass blocks determines the equivalent gravity center position of GCAM in the radial direction. When the two mass blocks are positioned symmetrically along the axis of the fuselage, the equivalent gravity center position of GCAM is attached to the axis of the fuselage. Thus, the glider could ascend or descend vertically. When the two mass blocks move towards each other, they cooperate as one, and work as a traditional GCAM of underwater gliders.

The mechanical parameters of TUG are shown in Table 1.

Table 1 Parameters of the tiny underwater glider

Characteristic	Description
Length	1.2 m
Diameter	0.164 m
Weight in air	18.3 kg
Communication	Free wave radio and GPS navigation
Battery	Lithium battery
DOFs of GCAM	3
Ballast capacity	0.276 kg

DOF: degree of freedom; GCAM: gravity center adjustment module

3 Modeling

Kinematic and dynamic models are presented to analyze the steering process with the presented method.

3.1 Coordinate and kinematic model

The coordinate frame consists of three parts (Fig. 4): inertial frame, body frame, and current frame. Inertial frame $\boldsymbol{E}_0(\boldsymbol{i}, \boldsymbol{j}, \boldsymbol{k})$ is identical with the Earth. The position and attitude of the glider are described as $\boldsymbol{b}=[x, y, z]^{\mathrm{T}}$ and $\boldsymbol{\theta}=[\phi, \theta, \psi]^{\mathrm{T}}$, respectively. The body frame $\boldsymbol{e}_0(\boldsymbol{x}_\mathrm{b}, \boldsymbol{y}_\mathrm{b}, \boldsymbol{z}_\mathrm{b})$ is identical with the glider itself. It is established at the buoyancy center. The translational and angular velocities in the body frame are $\boldsymbol{V}=[V_1, V_2, V_3]^{\mathrm{T}}$ and $\boldsymbol{\Omega}=[p, q, r]^{\mathrm{T}}$, respectively. In addition, the hydrodynamics is calculated in the current frame $\boldsymbol{\pi}_0(\boldsymbol{\pi}_1, \boldsymbol{\pi}_2, \boldsymbol{\pi}_3)$, which is obtained from the body frame by rotating around $\boldsymbol{y}_\mathrm{b}$ by attack angle α, and rotating around $\boldsymbol{z}_\mathrm{b}$ by sideslip angle β, where $\alpha=\arctan(V_3/V_1)$ and $\beta=\arcsin(V_2/\|\boldsymbol{V}\|)$.

The change rate of $\boldsymbol{b}$ is expressed as

$$\dot{\boldsymbol{b}}=\boldsymbol{R}_{\mathrm{EB}}\boldsymbol{V}. \tag{1}$$

With notations c=cos(·) and s=sin(·), $\boldsymbol{R}_{\mathrm{EB}}$ is expressed as

$$\boldsymbol{R}_{\mathrm{EB}}=\begin{bmatrix} \mathrm{c}\theta\mathrm{c}\psi & \mathrm{s}\phi\mathrm{s}\theta\mathrm{c}\psi-\mathrm{c}\phi\mathrm{s}\psi & \mathrm{c}\phi\mathrm{s}\theta\mathrm{c}\psi+\mathrm{s}\phi\mathrm{s}\psi \\ \mathrm{c}\theta\mathrm{s}\psi & \mathrm{c}\phi\mathrm{c}\psi+\mathrm{s}\phi\mathrm{s}\theta\mathrm{s}\psi & -\mathrm{s}\phi\mathrm{c}\psi+\mathrm{c}\phi\mathrm{s}\theta\mathrm{s}\psi \\ -\mathrm{s}\theta & \mathrm{s}\phi\mathrm{c}\theta & \mathrm{c}\phi\mathrm{c}\theta \end{bmatrix}. \tag{2}$$

The relationship between $\boldsymbol{\theta}$ and $\boldsymbol{\Omega}$ is expressed as

$$\dot{\boldsymbol{\theta}}=\begin{bmatrix} 1 & \mathrm{s}\phi\tan\theta & \mathrm{c}\phi\tan\theta \\ 0 & \mathrm{c}\phi & -\mathrm{s}\phi \\ 0 & \mathrm{s}\phi\sec\theta & \mathrm{c}\phi\sec\theta \end{bmatrix}\boldsymbol{\Omega}. \tag{3}$$

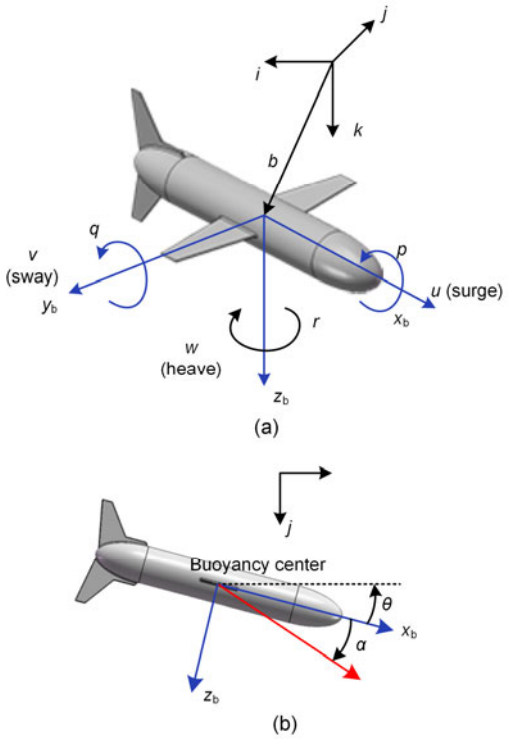

Fig. 4 Coordinate frame from the isometric view (a) and side view (b)

3.2 Dynamic model

A dynamic model describes the relationship between the motion and the forces on the vehicle. Dynamic models for underwater gliders have been

researched extensively (Zhang *et al.*, 2013). A dynamic model is presented as follows:

$$\dot{\boldsymbol{v}} = [\dot{\boldsymbol{V}}, \dot{\boldsymbol{\Omega}}]^{\mathrm{T}}. \tag{4}$$

The dynamic model in the body frame is shown as

$$\dot{\boldsymbol{v}} = \boldsymbol{M}^{-1}\left\{-\dot{\boldsymbol{M}}\boldsymbol{v} + \begin{bmatrix} \boldsymbol{P}\cdot\boldsymbol{\Omega} \\ \boldsymbol{\Pi}\cdot\boldsymbol{\Omega} + \boldsymbol{P}\cdot\boldsymbol{V} \end{bmatrix} + \begin{bmatrix} m_{\mathrm{n}} g(\boldsymbol{R}_{\mathrm{EB}}^{\mathrm{T}} k) \\ (m_{\mathrm{rb}}\boldsymbol{r}_{\mathrm{rb}} + m_{\mathrm{r}}\boldsymbol{r}_{\mathrm{r}}) g\cdot\boldsymbol{R}_{\mathrm{EB}}^{\mathrm{T}} k \end{bmatrix} + \begin{bmatrix} \boldsymbol{F} \\ \boldsymbol{T} \end{bmatrix}\right\}, \tag{5}$$

where $\boldsymbol{P}$ and $\boldsymbol{\Pi}$ are the translational and angular momentums mapped in the body frame, respectively, $\boldsymbol{M}$ is the generalized inertia matrix, $\boldsymbol{F}$ and $\boldsymbol{T}$ are the hydrodynamic forces and torques transformed to the body frame, respectively, m_{n} is the net weighted mass, m_{rb} and m_{r} are the mass of the static body and the mass block, respectively, $\boldsymbol{r}_{\mathrm{rb}}$ is the eccentric offset of the static body, and $\boldsymbol{r}_{\mathrm{r}}$ is the mass block from the origin of the body frame.

4 Hydrodynamics

4.1 Hydrodynamic model

Steering under an SPA always leads to a large attack angle. Thus, we present a hydrodynamic model for an underwater glider which is under either a low or a large attack angle. Attack angle is known to play an important role in supporting the lift force for a gliding glider. When the attack angle is smaller than the critical angle, the lift force increases with the attack angle. However, when the attack angle is beyond the critical angle, the lift force decreases when the attack angle increases. To demonstrate this characteristic, a hydrodynamic model is presented; this model is suitable for a wide range of attack angle α and sideslip angle β. The attack angle α ranges in (0°, 90°), and the sideslip angle β ranges in (0°, 90°). The presented model accommodates the hydrodynamics under both a low and a large attack angle.

The hydrodynamics consists of force $\boldsymbol{F}_{\mathrm{h}}$=$[-D, -\mathrm{SF}, -L]^{\mathrm{T}}$ and torque $\boldsymbol{T}_{\mathrm{h}}$=$[T_1, T_2, T_3]^{\mathrm{T}}$ in the current frame. The hydrodynamic forces and torques are expressed as

$$\begin{cases} D = (K_{\mathrm{D0}} + K_{\mathrm{D1}}\alpha + K_{\mathrm{D2}}\alpha^2 + K_{\mathrm{D3}}\alpha^3)V^a, \\ \mathrm{SF} = (K_{\mathrm{S0}} + K_{\mathrm{S1}}\beta + K_{\mathrm{S2}}\beta^2)V^b, \\ L = (K_{\mathrm{L0}} + K_{\mathrm{L1}}\alpha + K_{\mathrm{L2}}\alpha^2)V^c, \\ T_1 = (K_{\mathrm{p}}p + K_{\beta}\beta)V, \\ T_2 = (K_{\mathrm{MQ0}} + K_{\mathrm{MQ1}}\alpha + K_{\mathrm{MQ2}}\alpha^2)V^d + K_{\mathrm{Q}}qV, \\ T_3 = (K_{\mathrm{MY0}} + K_{\mathrm{MY1}}\beta + K_{\mathrm{MY2}}\beta^2)V^e + K_{\mathrm{R}}rV, \end{cases} \tag{6}$$

where V equals $\|\boldsymbol{V}\|$, a, b, c, d, and e have a reference value of 2, K_{β} equals zero for underwater gliders that are symmetric along the transection plane. D, SF, and L are caused by linear motion. Roll torque T_1 is caused by rotation. Pitch torque T_2 and yaw torque T_3 are caused by linear and rotatable motion, respectively.

The matrix $\boldsymbol{R}_{\mathrm{BC}}$ (Zhang *et al.*, 2013) is used to map the hydrodynamics from the current frame to the body frame:

$$\boldsymbol{F} = \boldsymbol{R}_{\mathrm{BC}}\boldsymbol{F}_{\mathrm{h}},\ \boldsymbol{T} = \boldsymbol{R}_{\mathrm{BC}}\boldsymbol{T}_{\mathrm{h}}. \tag{7}$$

The glider would have added mass $\boldsymbol{M}_{\mathrm{A}}$, inertia $\boldsymbol{I}_{\mathrm{A}}$, and cross term $\boldsymbol{C}_{\mathrm{A}}$ when it accelerates as a result of inviscid hydrodynamics.

The added mass, added inertia, and cross term are expressed as

$$\begin{cases} \boldsymbol{I}_{\mathrm{A}} = \mathrm{diag}(I_{\mathrm{A1}}, I_{\mathrm{A2}}, I_{\mathrm{A3}}), \\ \boldsymbol{M}_{\mathrm{A}} = \mathrm{diag}(M_{\mathrm{A1}}, M_{\mathrm{A2}}, M_{\mathrm{A3}}), \\ \boldsymbol{C}_{\mathrm{A}} = \begin{bmatrix} 0 & 0 & 0 \\ 0 & 0 & M_{\dot{w}} \\ 0 & N_{\dot{v}} & 0 \end{bmatrix}. \end{cases} \tag{8}$$

4.2 Hydrodynamic coefficients

The hydrodynamic coefficients have to be calculated to be applied in the hydrodynamic model. Hydrodynamics are classified into inviscid and viscous hydrodynamics. Different methods have been used to obtain the two types of hydrodynamic coefficients. Inviscid hydrodynamic coefficients are estimated by empirical equations based on the hypothesis of inviscid fluid (Isa *et al.*, 2014). The computational fluid dynamics (CFD) method is used to determine the viscous hydrodynamic coefficients. The CFD method discretizes the simulation domain with

meshed nodes, and uses a discretized Reynolds-averaged Navier–Stokes (RANS) method to calculate the coefficients. The procedure to obtain the viscous hydrodynamic coefficients is presented below.

4.2.1 Turbulence model

The RANS equation is used for the CFD simulation. Specifically, the standard k–ε turbulence model is used to calculate the hydrodynamic coefficients generated by the linear motion. The standard k–ω turbulence model is used to calculate the coefficients generated by the rotatable motion.

4.2.2 Simulation setup

The simulation is operated by the software Workbench. The simulation domain is set up by using the combination of a cuboid and a semi-cylinder. The cuboid volume is $3.5L_{\text{glider}}\cdot 4L_{\text{glider}}\cdot 4L_{\text{glider}}$, and the dimensions of the semi-cylinder are $4L_{\text{glider}}$ in diameter and $4L_{\text{glider}}$ in height (Fig. 5). The glider buoyancy center and the center of the semi-cylinder overlap. Thus, the simulation domain can be applied to cases with different attack and sideslip angles.

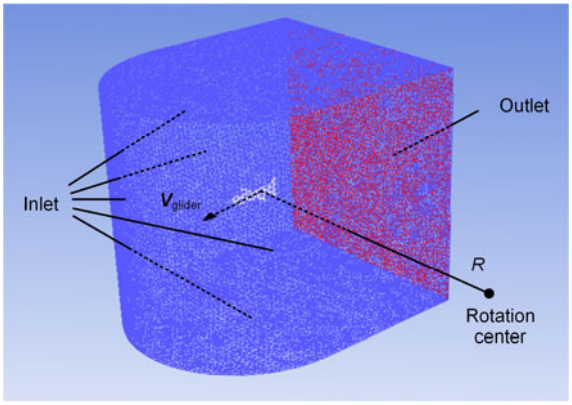

Fig. 5 Simulation domain for rotatable motions

For the simulation with the k–ε model, the boundaries are set as follows: the inlet boundary is set as the velocity inlet, where $\boldsymbol{V}_{\text{inlet}}$, whose components should be converted to the body frame, is specified according to Table 2. The outlet boundary is set as the pressure outlet, where the static pressure is zero; the glider surface is set as a no-slip wall.

For the simulation with the k–ω model, the simulation domain is set to be rotatable, where the frame motion option is selected. The angular speed of the fluid volume is $\boldsymbol{\omega}=\boldsymbol{V}_{\text{glider}}/R$, where $\boldsymbol{V}_{\text{glider}}$ is the linear velocity of the glider and R represents the rotation radius. The inlet boundary is the velocity boundary where all the velocity components are set to zero in their relative frames. The outlet boundary is the pressure boundary where the static pressure is set to zero.

Table 2 Parameters for computational fluid dynamics simulation

Model	Parameter
k–ε	$\|\|\boldsymbol{V}_{\text{inlet}}\|\| \in \{0.15, 0.30\}$ m/s $\alpha, \beta \in \{4°, 10°, 16°, 22°, 30°, 45°, 60°, 68°, 74°, 80°, 86°\}$
k–ω	$\|\|\boldsymbol{V}_{\text{glider}}\|\| \in \{0.15, 0.30\}$ m/s $\|\|\boldsymbol{\omega}\|\| \in \{0.025, 0.050, 0.075, 0.100\}$ rad/s

Hydrodynamics is analyzed in the current frame. Thus, the analysis of different α and β can be decoupled. The simulation is scheduled as follows: for the hydrodynamics generated by linear velocity, the individual values of α and β are 4°, 10°, 16°, 22°, 30°, 45°, 60°, 68°, 74°, 80°, and 86°, and the values of $\|\boldsymbol{V}_{\text{inlet}}\|$ are 0.15 and 0.3 m/s; for the hydrodynamics generated by rotation, the values of the angular speed $\|\boldsymbol{\omega}\|$ are 0.025, 0.05, 0.075, and 0.1 rad/s, and the values of the linear velocity $\|\boldsymbol{V}_{\text{glider}}\|$ at the glider buoyancy center are 0.15 and 0.3 m/s. The simulation parameters are listed in Table 2.

4.2.3 Data fitting

The velocity path line of linear motion under an attack angle of 86° is shown in Fig. 6. Fig. 7 illustrates the simulation results of forces and torques. The simulations based on the k–ε model are used to estimate the forces and torques generated by linear velocity. The drag force D, lift force L, and pitch moment M_{P} that are mapped in the current frame are relevant to α. The side force SF and yaw moment M_{Y} that are mapped in the current frame are relevant to β. The drag torques around roll, pitch, and yaw axises are relevant to the angular speed.

Fig. 7 shows that L and M_{P} are positively relevant to α before α reaches the critical angle, which is close to 45°. When α is beyond the critical angle, L and M_{P} have a negative correlation with α. A critical angle for β exists at approximately 45°, thereby changing the increase rate of side force SF. Results indicate that the model fits the observations well.

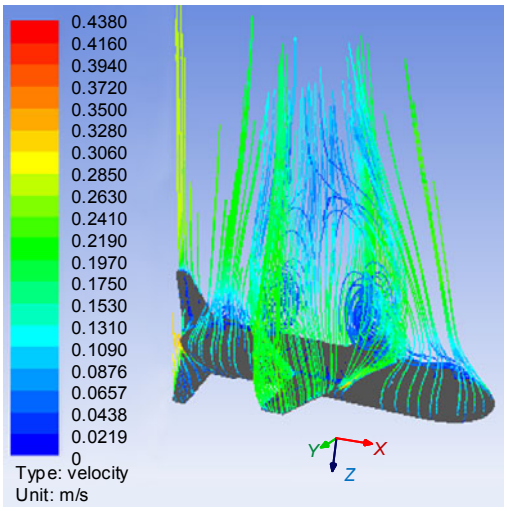

Fig. 6 Velocity path line of linear motion under attack angle 86°

The inviscid hydrodynamics are estimated by using the empirical method (Isa *et al.*, 2014), which uses the length and radius of the hull to estimate the main added mass and added inertia.

The hydrodynamic coefficients of TUG are shown in Table 3.

Table 3 Hydrodynamic coefficient list

Symbol	Value
$\boldsymbol{M}_{\mathrm{A}}$	diag(0.41, 8.23, 11.36) kg
N_{v}	0.45 kg/m
K_{D0}	4.05 kg/m
K_{D2}	80.72 kg/(m·rad^2)
a	1.51
K_{S1}	−37.35 kg/(m·rad)
b	1.64
K_{L1}	147.05 kg/(m·rad)
c	1.77
K_{MQ0}	0.29 kg
K_{MQ2}	−20.46 kg/rad^2
d	1.86
K_{MY1}	1.93 kg/rad
K_{R}	−12.96 kg·s/rad
$\boldsymbol{I}_{\mathrm{A}}$	diag(0.09, 0.75, 0.82) kg·m^2
M_{w}	0.61 kg·m
K_{D1}	2.01 kg/(m·rad)
K_{D3}	−36.12 kg/(m·rad^3)
K_{S0}	0.34 kg/m
K_{S2}	23.42 kg/(m·rad^2)
K_{L0}	0.73 kg/m
K_{L2}	−96.54 kg/(m·rad^2)
K_{P}	−7.85 kg·s/rad
K_{MQ1}	31.89 kg/rad
K_{Q}	−8.26 kg·s/rad
K_{MY0}	0.11 kg
K_{MY2}	8.98 kg/rad^2
e	2.11

5 Characteristic analysis

The steering process with or without an SPA could be simulated with the presented model and the calculated hydrodynamic coefficients. The simulation could help us understand how different parameters influence the steering performance under or not under an SPA. The net buoyancy and roll angle are addressed to find the optimal input parameters in the case of steering under an SPA. The variable pitch angle is addressed to elucidate how steering under an SPA works better than that not under an SPA in a space-saving field.

The simulation concentrates on the continuous steering process. To quantify the space-saving effects for different steering cases, a measurable indicator, the steering ratio, has been introduced. The steering ratio equals the result of dividing the steered angle by the vertical displacement over which the glider glides. It indicates the steered angle in unit vertical displacement for an underwater glider.

An attitude closed-loop controller is used to maintain the pitch angle and the roll angle at a specified value under different net buoyancies (Fan and Woolsey, 2014). The controller is composed of a feedforward loop and feedback loop.

Steering under an SPA aims to achieve a large steering angle when occupying a small vertical displacement as the underwater glider steers.

5.1 Simulation setup

The simulation of motion characteristics of the TUG can be derived based on dynamic and hydrodynamic models using MATLAB. The nonlinear dynamic equations in the simulation are solved by MATLAB ode45 subroutine.

5.2 Longitudinal comparison

Longitudinal comparison simulation is aimed to find the optimal net buoyancy and the roll angle, which are subject to the mechanical limit, to achieve the highest steering ratio. In the simulation under an SPA, the net buoyancy is set at −0.068, −0.102, and

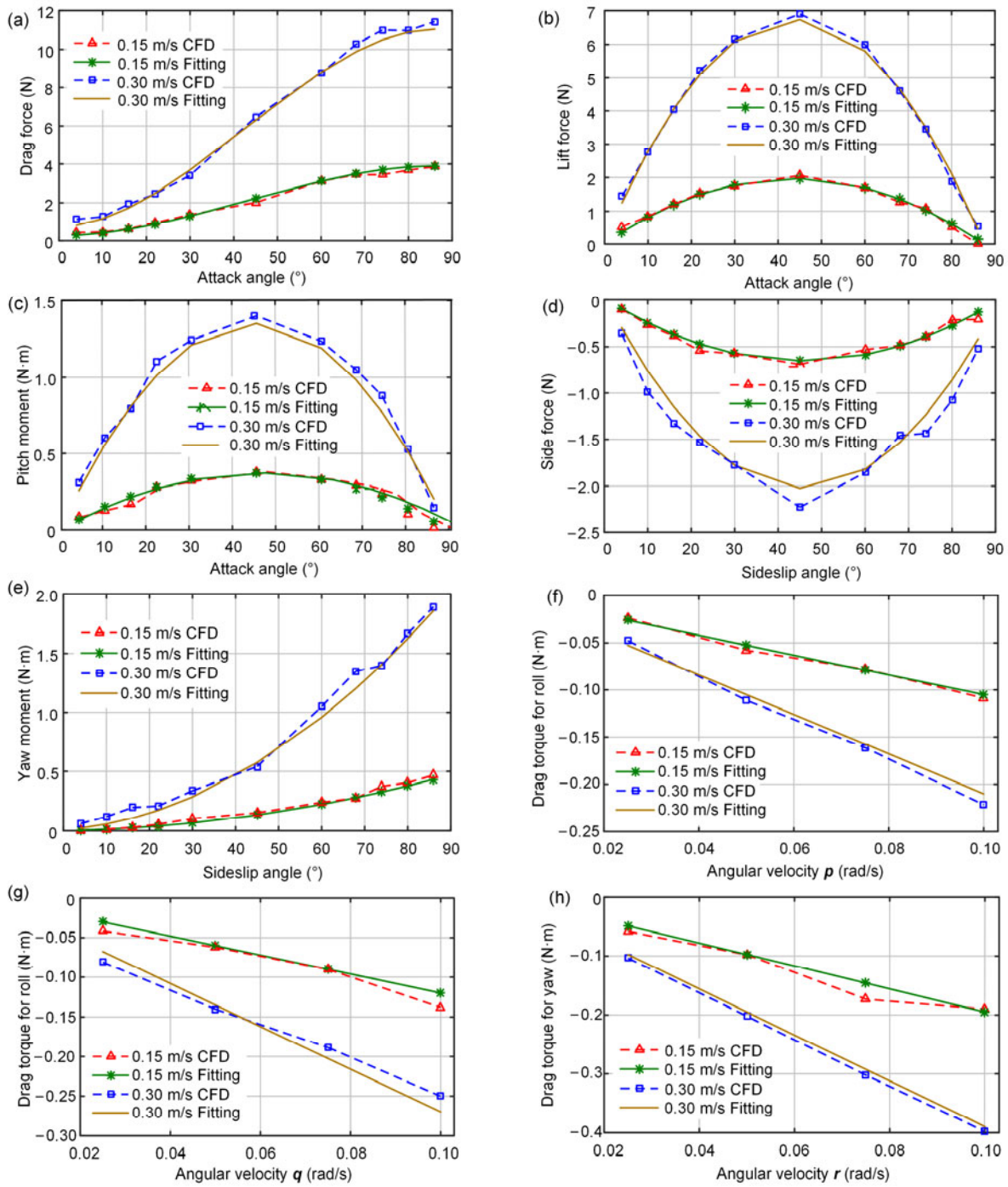

Fig. 7 Hydrodynamics with computational fluid dynamics results and curve fitting results: (a) drag force; (b) lift force; (c) pitch moment; (d) side force; (e) yaw moment; (f) drag torque for roll; (g) drag torque for pitch; (h) drag torque for yaw

−0.136 kg, the roll angle is set at −10°, −25°, and −40°, and the pitch angle is set at −1°. To ensure that the results of different cases are comparable, each simulation case shares the same vertical descending displacement (8 m). The initial linear velocity is (0.02, 0) m/s, and the initial rotational velocity is 0 in all cases.

Fig. 8 shows the depth and steering orientation in the steering process with a net buoyancy of −0.068 kg and a roll angle of −40°. Table 4 shows the attack

angle and the steering ratio for each case. The attack angle column shows that in all cases, the glider glides with an attack angle greater than the critical angle of 45°, which means that the flights are under large attack angles. The steering ratio column shows that the steering ratio increases with the magnitude of net buoyancy and roll angle. The highest two steering ratio values occur in cases A-6 and A-9. Though case A-9 scores higher than case A-6 on the steering ratio, the gap is small compared with the extra energy that is consumed to increase the net buoyancy for case A-9. Thus, the parameters in case A-6 are chosen as the optimal parameters for steering under an SPA with a net buoyancy of −0.102 kg and a roll angle of −40°.

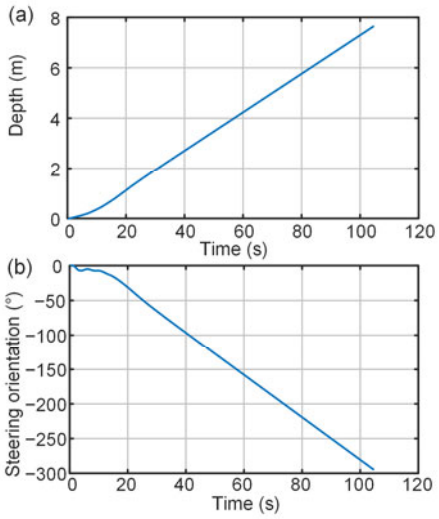

Fig. 8 Simulated data for case A-3: (a) depth; (b) steering orientation

Table 4 Simulation results of the continuous steering process

Case ID	Net buoyancy (kg)	Roll angle (°)	Attack angle (°)	Steering ratio (°/m)
A-1	−0.068	−10	81.4	7.6
A-2	−0.068	−25	76.2	17.6
A-3	−0.068	−40	73.3	39.1
A-4	−0.102	−10	80.7	8.8
A-5	−0.102	−25	74.5	21.4
A-6	−0.102	−40	72.3	43.3
A-7	−0.136	−10	79.1	9.2
A-8	−0.136	−25	73.7	22.9
A-9	−0.136	−40	70.8	43.7

5.3 Lateral comparison

The lateral comparison simulation is aimed to obtain the steering ratio of TUG under or not under an SPA. The pitch angle is sequently set at −1°, −20°, and −40°, the net buoyancy is −0.102 kg, and the roll angle is −40°. The initial conditions and constraints are the same as those in the longitudinal comparison simulations where the rotational velocity is 0 in all cases.

Table 5 shows the simulation results for case B-1 where the glider steers under an SPA, and cases B-2 and B-3 where the glider does not. Steering under an SPA obviously increases the steering ratio and the attack angle. Case B-1 under an SPA has the highest steering ratio, which is 2.5 times that in case B-2, and 7.3 times that in case B-3.

Table 5 Simulation results for steering with a small pitch angle (case B-1) and without a small pitch angle (cases B-2 and B-3)

Case ID	Pitch angle (°)	Attack angle (°)	Steering ratio (°/m)
B-1	−1	72.3	43.3
B-2	−20	6.7	17.3
B-3	−40	3.2	5.9

6 Trial

A lake trial was conducted to investigate the space-saving advantage of steering under an SPA and the accuracy of the simulation results. The trial was conducted in a lake in Zhejiang Province, China (Fig. 9). The trial included two parts: continuous steering and waypoint flight. In the trial, the depth and Euler angle states of TUG were recorded for analysis when lacking other velocity-related states.

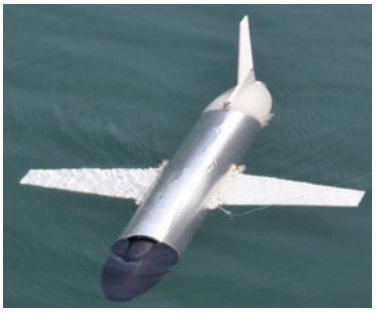

Fig. 9 Lake trial

6.1 Continuous steering

Continuous steering aims to investigate the steering ratio of TUG under or not under an SPA.

All the trial tests were conducted with the parameters simulated in cases A-1–A-9 from Table 4 and cases B-1–B-3 from Table 5. In each case, the glider worked as follows:

1. The pitch angle and roll angle are adjusted to the specified value on the surface.

2. The net buoyancy is adjusted to the specified value.

3. Steering is performed continuously when descending with the specified parameters.

4. Steering is stopped when the depth reaches 8 m, and then the glider ascends to feed back the recorded data.

All the cases were run for three times. The run with the median steering ratio value for each case would be kept for analysis.

The trialed gliding states for cases B-1–B-3 are shown in Fig. 10. The steering orientation values for each case were translated with the same initial value. Case B-3 took 35 s to reach 8 m. Thus, Fig. 10 presents the data of the first 35 s.

Fig. 10 shows that the average steering angular velocity for case B-1 is 1.5 times that in case B-2, and 2.5 times that in case B-3. Fig. 10 shows that the vertical displacement for case B-1 is 0.6 times that in case B-2, and 0.36 times that in case B-3. These findings indicate that steering with an SPA not only saves time for steering, but also takes up less vertical displacement than steering without an SPA.

A comparison between the simulation and trial for case B-1 is shown in Fig. 11. The simulated depth is approximately 12.5% smaller than the experimental result. The simulation result for steering orientation is 11.2% smaller than the experimental result. Fig. 11 shows that the accuracy of the simulation is acceptable. The calculated results of the steering ratio for each case are shown in Fig. 12.

In Fig. 12a, the steering ratio increases with the magnitude of net buoyancy and roll angle, which agrees with the simulation results of cases A-1–A-9. In addition, a comparison between the trial and the simulation results shows that the presented model has a maximum relative error of 11.1%. Therefore, the presented model works well under a large attack angle.

Fig. 12b shows that the steering with an SPA (pitch −1°) achieves a higher steering ratio than in the control cases. The case with an SPA has the highest steering ratio, which is 2.6 times that in case B-2, and 7.3 times that in case B-3. Results show that steering under an SPA has good space-saving performance.

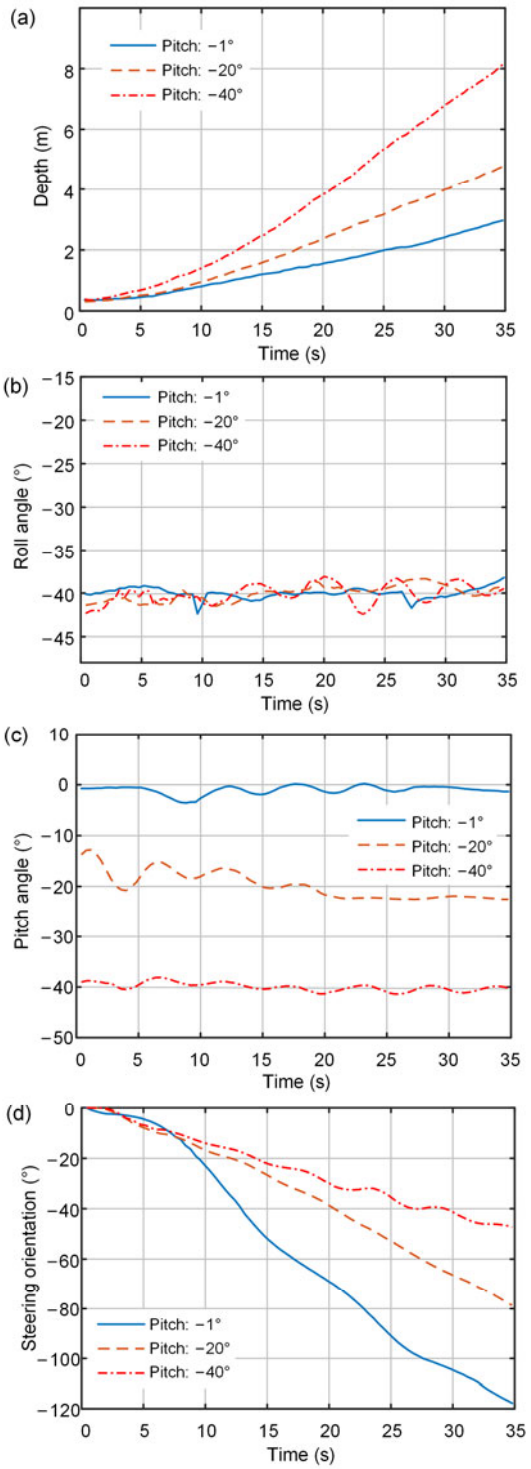

Fig. 10 Gliding states for cases B-1–B-3: (a) depth; (b) roll angle; (c) pitch angle; (d) steering orientation

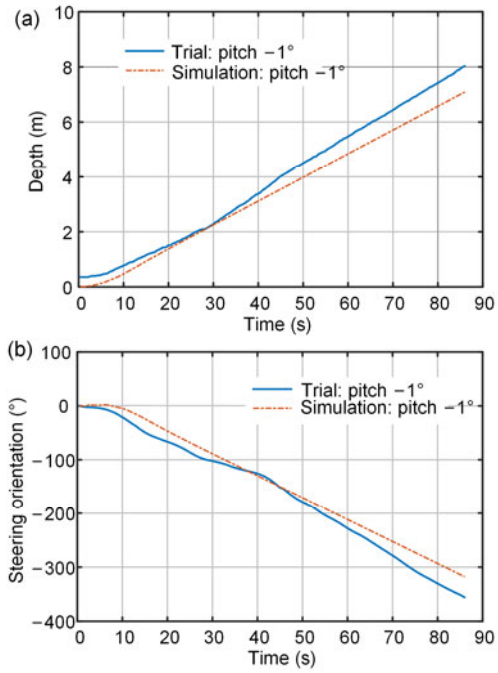

Fig. 11 Trialed and simulated gliding states for case B-1: (a) depth; (b) steering orientation

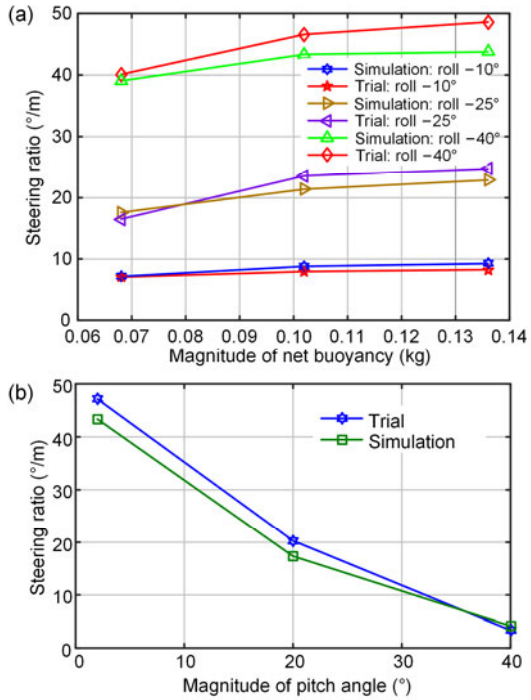

Fig. 12 Steering ratio for simulation and trial of cases A-1–A-9 (a) and cases B-1–B-3 (b)

6.2 Waypoint flight

Steering under an SPA has good space-saving performance and could therefore be applied to waypoint flight. The waypoint flight trial consisted of two groups, each including four waypoints. Group A steered under an SPA, while group B steered with a pitch angle of −20°. Waypoints were connected by a single flight and vertical monitoring. The waypoint flight trial was aimed to compare the total horizontal displacements along the target orientation between the flights under an SPA and those not under an SPA for the steering process. The trial was conducted as follows:

1. The trial is initialized with the specified location and steering orientation. The GPS fix is recorded as waypoint 1.

2. The steerings on orientation 180° (southing) under and not under an SPA are followed.

3. A transit glide with a pitch angle of −20° is performed until the glider reaches the depth of 35 m.

4. Vertical ascent to the surface is performed.

5. The GPS fix is recorded as the next waypoint, and the recorded data are posted back.

6. Steps 2–5 are repeated until the number of waypoints reaches four.

The real-time steering orientation of the single flight between waypoints 1 and 2 is shown in Fig. 13. The steering process with an SPA occupies only 6.6 m of the vertical displacement, while the control case occupies 14.4 m. It means that the flight that steers under an SPA left more vertical space for the transit flight process than in the control case.

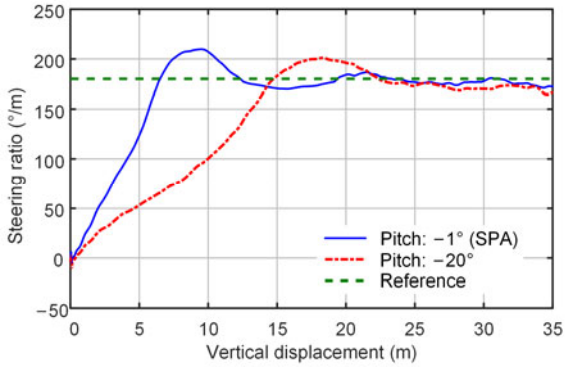

Fig. 13 Steering orientation of single flight under pitch −1° (SPA: small pitch angle) and −20°

With the GPS fixes of waypoints, the southing horizontal displacement covered by the flights can be calculated. The displacement is calculated by the developed software shown in Fig. 14, where the waypoint displacements are decomposed into north

orientation (upward) and east orientation (rightward), and dN and dE are the deviations in the north and east orientations, respectively. In the flight that combines an SPA, the southing horizontal displacements between waypoints are 47.6, 52.2, and 48.2 m, with a total of 148.0 m. In the flight that is not steered under an SPA, the southing horizontal displacements between waypoints are 34.2, 37.3, and 39.3 m, with a total of 110.8 m. The flight steering under an SPA covers a 33.5% larger southing horizontal displacement than that not under an SPA. Thus, steering under an SPA helped TUG leave more vertical space for transit flight, to ensure that the flight could cover a larger horizontal displacement than the control group.

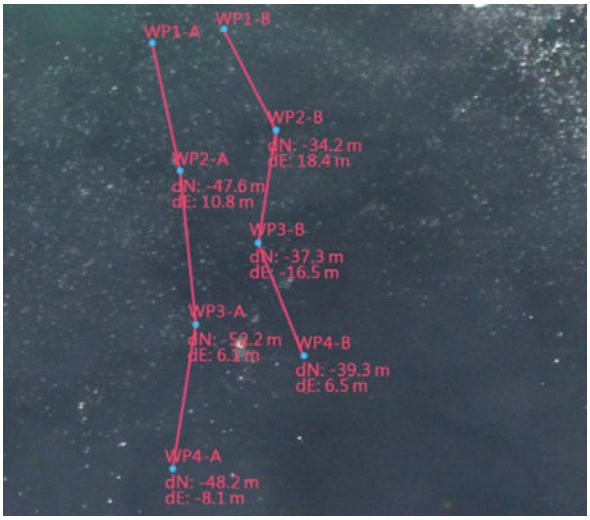

Fig. 14 Waypoints with GPS handle

Even though steering under an SPA leads to a high steering ratio and a high angular velocity, and could be used in waypoint monitoring, there may exist some trade-offs steering under an SPA. First, underwater gliders may be vulnerable when the gliding velocity is significantly lower than that of the currents. The steering pitch angle is suggested to be compromised to increase the velocity when steering in areas with non-ignorable currents. Second, steering under a large attack angle may suffer from local turbulences, which may cause the glider to vibrate. It might be okay for general monitoring. However, it is a problem for vibration-sensitive monitoring. Gliding strategies have to be balanced between adapting to certain conditions and enhancing the steering ratio.

7 Conclusions

This paper presents a space-saving steering method under an SPA for appearance-fixed underwater gliders. A viscous hydrodynamic model is amended to extend its applicability for a large attack angle. A computational method based on a computational fluid simulation is used to determine the hydrodynamic coefficients. An analysis is conducted to evaluate the effect of steering under an SPA under different net buoyancies, roll angles, and pitch angles. The continuous steering test shows that steering under an SPA has good space-saving performance with an optimal net buoyancy of −0.102 kg and a roll angle of −40°. Moreover, a comparison between the simulations and experiments shows that the amended model predicts the steering ratio accurately with a maximum relative error of 11.1%. A flight test shows the applicability of steering under an SPA to multiple-waypoint flights. In the waypoint flight test, the flight that combines an SPA covers a 33.5% larger southing horizontal displacement than that in the control case. Results indicate that steering under an SPA could be applied to lake monitoring to enlarge the monitoring area.

Reference

Ahmadzadeh, S.R., Kormushev, P., Caldwell, D.G., 2014. Multi-objective reinforcement learning for AUV thruster failure recovery. IEEE Symp. on Adaptive Dynamic Programming and Reinforcement Learning, p.1-8. http://dx.doi.org/10.1109/ADPRL.2014.7010621

Austin, J., 2013a. Observations of near-inertial energy in Lake Superior. *Limnol. Ocean.*, **58**(2):715-728. http://dx.doi.org/10.4319/lo.2013.58.2.0715

Austin, J., 2013b. The potential for autonomous underwater gliders in large lake research. *J. Great Lake Res.*, **39**(Supplement 1):8-13. http://dx.doi.org/10.1016/j.jglr.2013.01.004

Bardyshev, V.I., 2004. Testing underwater bottom-moored antenna arrays in the sea and in a man-made lake. *Acoust. Phys.*, **50**(6):641-646. http://dx.doi.org/10.1134/1.1825092

Caffaz, A., Caiti, A., Casalino, G., *et al*., 2010. The hybrid glider/AUV folaga. *IEEE Robot. Autom. Mag.*, **17**(1): 31-44. http://dx.doi.org/10.1109/MRA.2010.935791

Cao, J.J., Cao, J.L., Yao, B.H., *et al*., 2015. Three dimensional model, hydrodynamics analysis and motion simulation of an underwater glider. OCEANS, p.1-8. http://dx.doi.org/10.1109/OCEANS-Genova.2015.7271365

Chen, Y., Lu, C.J., Guo, J.H., 2010. Numerical study of the cavitating flows over underwater vehicle with large angle of attack. *J. Hydrodyn.*, **22**(5):893-898. http://dx.doi.org/10.1016/S1001-6058(10)60048-0

Denkenberger, J.S., Driscoll, C.T., Effler, S.W., *et al*., 2007. Comparison of an urban lake targeted for rehabilitation and a reference lake based on robotic monitoring. *Lake Reserv. Manag.*, **23**(1):11-26. http://dx.doi.org/10.1080/07438140709353906

Fan, S., Woolsey, C.A., 2014. Dynamics of underwater gliders in currents. *Ocean Eng.*, **84**:249-258. http://dx.doi.org/10.1016/j.oceaneng.2014.03.024

Geisbert, J.S., 2005. Underwater Gliders: Dynamics, Control and Design. PhD Thesis, Princeton University, Princeton, USA.

Geisbert, J.S., 2007. Hydrodynamic modeling for Autonomous Underwater Vehicles Using Computational and Semi-Empirical Methods. MS Thesis, Virginia Polytechnic Institute and State University, Blacksburg, USA.

He, R., Wooller, M.J., Pohlman, J.W., *et al*., 2012. Diversity of active aerobic methanotrophs along depth profiles of Arctic and Subarctic lake water column and sediments. *ISME J.*, **6**(10):1937-1948. http://dx.doi.org/10.1038/ismej.2012.34

Hussain, N.A.A., Arshad, M.R., Mohd-Mokhtar, R., 2011. Underwater glider modelling and analysis for net buoyancy, depth and pitch angle control. *Ocean Eng.*, **38**(16): 1782-1791. http://dx.doi.org/10.1016/j.oceaneng.2011.09.001

Isa, K., Arshad, M.R., 2011. Motion simulation for propeller-driven USM underwater glider with controllable wings and rudder. 2nd Int. Conf. on Instrumentation Control and Automation, p.316-321. http://dx.doi.org/10.1109/ICA.2011.6130179

Isa, K., Arshad, M.R., Ishak, S., 2014. A hybrid-driven underwater glider model, hydrodynamics estimation, and an analysis of the motion control. *Ocean Eng.*, **81**:111-129. http://dx.doi.org/10.1016/j.oceaneng.2014.02.002

Ivanov, A.V., Gladkochub, D.P., Déverchère, J., *et al*., 2013. Introduction to special issue: geology of the Lake Baikal region. *J. Asian Earth Sci.*, **62**:1-3. http://dx.doi.org/10.1016/j.jseaes.2012.12.010

Jones, C., Allsup, B., DeCollibus, C., 2014. Slocum glider: expanding our understanding of the oceans. OCEANS, p.1-10. http://dx.doi.org/10.1109/OCEANS.2014.7003260

Leonard, N.E., Paley, D.A., Davis, R.E., *et al*., 2010. Coordinated control of an underwater glider fleet in an adaptive ocean sampling field experiment in Monterey Bay. *J. Field Rob.*, **27**(6):718-740. http://dx.doi.org/10.1002/rob.20366

Li, Y., Gal, G., Makler-Pick, V., *et al*., 2014. Examination of the role of the microbial loop in regulating lake nutrient stoichiometry and phytoplankton dynamics. *Biogeosciences*, **11**(11):2939-2960. http://dx.doi.org/10.5194/bg-11-2939-2014

Lim, D.S.S., Brady, A.L., Abercromby, A.F., *et al*., 2011. A historical overview of the pavilion lake research project—analog science and exploration in an underwater environment. *GSA Spec. Papers*, **483**:85-116. http://dx.doi.org/10.1130/2011.2483(07)

Mahmoudian, N., Geisbert, J., Woolsey, C., 2010. Approximate analytical turning conditions for underwater gliders: implications for motion control and path planning. *IEEE J. Ocean. Eng.*, **35**(1):131-143. http://dx.doi.org/10.1109/JOE.2009.2039655

Peng, S.L., Yang, C.J., Fan, S.S., *et al*., 2014. Hybrid underwater glider for underwater docking: modeling and performance evaluation. *Mar. Technol. Soc. J.*, **48**(6): 112-124. http://dx.doi.org/10.4031/MTSJ.48.6.5

Suberg, L., Wynn, R.B., van der Kooij, J., *et al*., 2014. Assessing the potential of autonomous submarine gliders for ecosystem monitoring across multiple trophic levels (plankton to cetaceans) and pollutants in shallow shelf seas. *J. Meth. Ocean.*, **10**:70-89. http://dx.doi.org/10.1016/j.mio.2014.06.002

Wang, C.T., Yu, J.C., Wu, L.H., *et al*., 2007. Research on movement mechanism simulation and experiment of underwater glider. *Ocean Eng.*, **25**(1):64-69. http://dx.doi.org/10.16483/j.issn.1005-9865.2007.01.010

Wang, L.F., Yang, L.Y., Kong, L.H., *et al*., 2014. Spatial distribution, source identification and pollution assessment of metal content in the surface sediments of Nansi Lake, China. *J. Geochem. Exp.*, **140**:87-95. http://dx.doi.org/10.1016/j.gexplo.2014.02.008

Wang, Y.H., Zhang, H.W., Wang, S.X., 2009. Trajectory control strategies for the underwater glider. Int. Conf. on Measuring Technology and Mechatronics Automation, p.918-921. http://dx.doi.org/10.1109/ICMTMA.2009.617

Weng, Y., Yang, H., He, J.Y., *et al*., 2015. Microstructure measurement form an underwater glider: motion analysis and experimental results. OCEANS, p.1-5. http://dx.doi.org/10.1109/OCEANS-Genova.2015.7271488

Yang, C.J., Peng, S.L., Fan, S.S., 2014. Performance and stability analysis for ZJU glider. *Mar. Technol. Soc. J.*, **48**(3):88-103. http://dx.doi.org/10.4031/MTSJ.48.3.6

Zhang, F.T., Zhang, F.M., Tan, X.B., 2014. Tail-enabled spiraling maneuver for gliding robotic fish. *J. Dynam. Syst. Meas. Contr.*, **136**(4):041028. http://dx.doi.org/10.1115/1.4026965

Zhang, S.W., Yu, J.C., Zhang, A.Q., *et al*., 2013. Spiraling motion of underwater gliders: modeling, analysis, and experimental results. *Ocean Eng.*, **60**:1-13. http://dx.doi.org/10.1016/j.oceaneng.2012.12.023

doi: 10.1631/FITEE.1500399

题目：适用于湖水监测的水下滑翔机的空间高效转向方法

概要：越来越多的水下滑翔机正在被应用到湖水监测中。由于湖水具有有限的竖直空间，为了让水下滑翔机能够扩大不同监测点的间距，水下滑翔机应具有空间高效的转向能力。本文提出一种使用小俯仰角的转向方法，以便让外形固定的水下滑翔机能够具有空间高效的转向能力。使用小俯仰角转向可以提高水下滑翔机在单位竖直空间下的转向角度。本文提出了一种同时适用于大小攻角的水下滑翔机水动力模型，对小俯仰角转向过程中最优的净浮力与横滚角度展开了研究。为了验证水动力模型和转向方法的适用性，研制了小型水下滑翔机原型机并进行了湖水试验。试验表明，水下滑翔机使用小俯仰角进行转向比使用大俯仰角转向更能节省竖直方向消耗的空间。仿真结果与湖水试验结果一致。另外，多监测点连续监测试验表明，与比不使用小俯仰角转向相比，水下滑翔机使用小俯仰角进行转向能够覆盖更大的监测区域。

关键词：水下滑翔机；湖水监测；空间高效；转向方法；小俯仰角；水动力